PHYSICAL REVIEW APPLIED **22,** 034030 (2024)

Editors' Suggestion

Magnetic induction sensor based on a dual-frequency atomic magnetometer

Hengyan Wang,[1,2] Michael Zugenmaier,[1] Kasper Jensen,[1,3] Wenqiang Zheng,[1,4,*] and
Eugene S. Polzik[1,†]

[1] *Niels Bohr Institute, University of Copenhagen, Blegdamsvej 17, Copenhagen Ø 2100, Denmark*
[2] *Department of Physics, Zhejiang University of Science and Technology, Hangzhou 310023, China*
[3] *School of Physics and Astronomy, University of Nottingham, University Park, Nottingham NG7 2RD, United Kingdom*
[4] *Zhejiang Provincial Key Laboratory and Collaborative Innovation Center for Quantum Precision Measurement, College of Science, Zhejiang University of Technology, Hangzhou 310023, China*

(Received 6 April 2024; revised 3 July 2024; accepted 26 August 2024; published 12 September 2024)

We propose and demonstrate a combined static- and oscillating-field alkali atom magnetometer and use it as a magnetic induction tomography sensor. The magnetometer realizes simultaneous measurements of the static and oscillating magnetic fields using two different Zeeman transitions of a single sensor. This approach dramatically enhances the long-term stability and sensitivity of detection of low-conductivity objects. Using our dual-frequency magnetometer, we detect small containers with salt water with conductivity as low as 0.55 S/m. We achieved a conductivity measurement uncertainty of 0.18 S/m with a 10-s integration time. This performance is sufficient to distinguish between healthy and malignant tissue in the human body. The dual-frequency magnetometer can also be used as a self-stabilized radio-frequency magnetometer.

DOI: 10.1103/PhysRevApplied.22.034030

I. INTRODUCTION

Optically pumped magnetometers (OPMs) utilize optical pumping and probing of atomic systems such as rubidium or cesium atomic vapor for highly sensitive measurements of the magnetic field [1–3]. Biomagnetic measurements with OPMs are promising for noninvasive medical diagnostics, and detection of various weak magnetic fields such as from the human brain [4,5], heart [6–9], muscle [10,11], eye [12], and nerves [13,14] have been demonstrated. OPMs can also be used for detecting rf magnetic fields [15–17] and have in recent years started to attract fast-growing interest as an alternative technique to measure induced magnetic fields in the context of magnetic induction tomography (MIT) [18–23]. In MIT measurement, eddy currents are induced by placing the object of interest in the so-called primary rf magnetic field. The electrical and magnetic properties of the object can be investigated by measuring the secondary rf field generated by eddy currents.

In the context of MIT, OPMs have several advantages compared to the commonly used induction coils. In particular, their operating frequencies are readily tuned by varying the bias magnetic field and their sensitivities are fundamentally independent of the operating frequency. OPM-based eddy-current detection [24–26] has been demonstrated in different application scenarios such as for nondestructive testing [27,28], edge and hole detection [29,30], object identification [31], and remote sensing [32,33]. One of the most attractive and challenging application is MIT of the heart [34]. It potentially enables a contactless and noninvasive method for cardiac diagnosis. To this end, we must rise to the challenge of enabling the atomic magnetometers to stably measure electrical conductivities smaller than 1 S/m with high SNR. Many efforts have brought OPM close to the regime applicable for the heart MIT. A differential technique improved the SNR by more than 3 orders of magnitude and achieved conductivity measurement as low as 4 S/m [35]. In a recent report, a conductivity measurement of 0.91 S/m was demonstrated in an unshielded environment [36].

To further explore the potential of OPMs in MIT application, the stability of a sensor becomes a critical issue. The strength of the secondary magnetic field generated by the eddy current is proportional to the operating frequency, which for an OPM is determined by the bias magnetic field B_0. The fluctuations of the electrical current in the coil generating B_0 become a severe technical problem when the operating frequency is high. In the unshielded environment, the fluctuation of the ambient magnetic field also

---

[*] Contact author: wqzheng@zjut.edu.cn
[†] Contact author: polzik@nbi.ku.dk

contributes to the instability. Such fluctuations affect the long-term performance of OPMs and therefore limit the benefit from offline averaging and the application of OPMs for multidimensional MIT. Active stabilization of the bias magnetic field with a closed-loop compensation system is frequently used to mitigate the problem and can be implemented using one or more auxiliary fluxgate magnetometers [27,36–39]. Such stabilization systems could potentially be improved by reducing the distance between the atomic vapor cell and the fluxgate, which otherwise results in the inaccuracy of the field compensation. However, a fluxgate will never be able to be colocated with an OPM, and a too close distance between the fluxgate and the OPM could also lead to magnetic field noise affecting the OPM due to the fluxgate electronics. In addition, the sensitivity of the fluxgate limits the compensation precision and the requirement of additional instruments hampers the development of a compact MIT sensor. Recently, a single OPM based on two rubidium isotopes in the same vapor cell was used to stabilize the static bias magnetic field while simultaneously measuring rf magnetic fields [40].

Here we propose an alternative dual static- and oscillating-field magnetometer based on the nonlinear Zeeman splittings in the ground state ($F = 4$) of cesium atoms. We use the resonance signal of the Zeeman transition $m = 2 \leftrightarrow 3$ as the error signal to actively control the bias magnetic field via a PID closed-loop feedback system. Meanwhile, we extract the conductivity information from the resonance signal of Zeeman transition $m = 3 \leftrightarrow 4$. The single-species feature allows accurate compensation of the bias magnetic field, without the error coming from the difference in positions of the main and the additional magnetic sensors. The stabilization system greatly improves the long-term stability of the setup and allows more benefits from signal averaging. Moreover, we propose and demonstrate a practical method to optimize the rf OPM with an oscillating field mimicking the magnetic field from the eddy current. Utilizing our dual-frequency magnetometer technology, we have successfully detected small containers filled with salt water, even with conductivity levels as low as 0.55 S/m. It came with an uncertainty on the conductivity measurement of 0.18 S/m for an integration time of 10 s.

II. OPM-BASED DETECTION OF LOW-CONDUCTIVITY SAMPLES

The schematic of the setup is shown in Fig. 1. The sensor of our rf magnetometer is a 5-mm cubic paraffin-coated cesium vapor cell. Circularly polarized light from two lasers denoted “pump” and “repump” optically polarizes the cesium atoms in the x direction along the dc bias magnetic field. The repump laser works on atoms decaying to $F = 3$ and drives them back to $F = 4$, while the pump laser drives atoms in $F = 4$ to the Zeeman sublevel $m = 4$. Linearly polarized “probe” light measures the projection J_z of the collective atomic spin in the probe propagation direction and thereby the rf magnetic field at the sensor location. Additional details about the setup can be found in Ref. [35]. The magnetometer scheme is based on magnetic resonance. Cesium atoms are placed in a combination of a static magnetic field $\mathbf{B_0} = B_0\hat{\mathbf{x}}$ and a transverse magnetic field $\mathbf{B}_{\rm rf}$ along the y direction oscillating at a frequency ω close to the Larmor frequency $\omega_L = \gamma B_0$, where γ is the cesium gyromagnetic ratio. In general, the oscillating field can be written as $\mathbf{B}_{\rm rf} = [B_c \cos(\omega t) + B_s \sin(\omega t)]\,\hat{\mathbf{y}}$. Through the solution to the Bloch equation, we can obtain the out-phase amplitude J_{qu} and in-phase amplitude J_{ip}

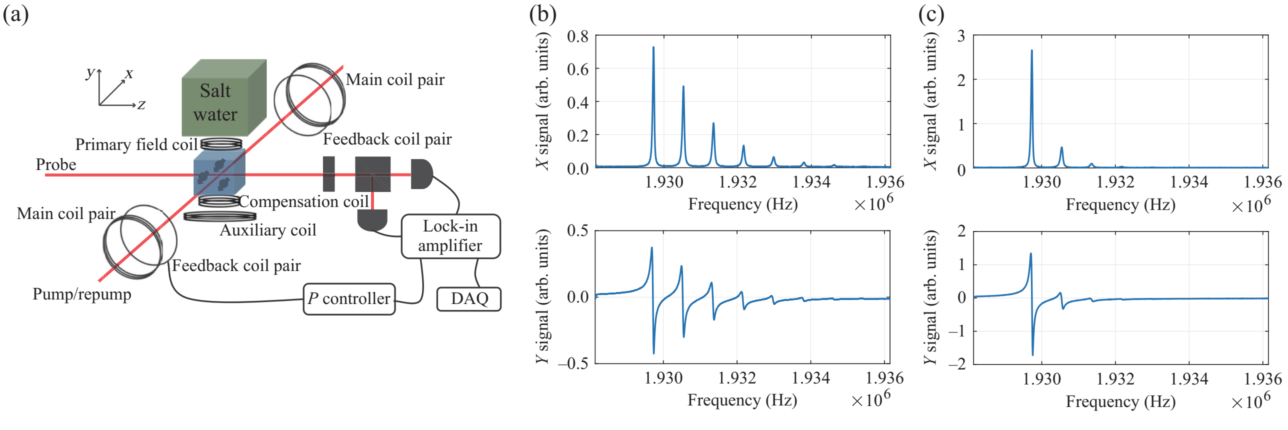

FIG. 1. Experimental setup and MORSs of the cesium vapor cell. (a) Schematics of the experimental setup. The vapor cell, coils, and salt-water container are placed inside a cylindrical magnetic shield (not shown). Lasers, the detector, and electronics are placed outside the magnetic shield. (b) MORS of the cesium atomic ensemble with only repump laser on, corresponding to 81.3% atomic polarization. (c) MORS of the cesium atomic ensemble with both pump and repump lasers on, corresponding to 96.4% atomic polarization. The upper and lower MORSs are out-of-phase and in-phase outputs of LIA, respectively. The left-most line relates to the Zeeman transition $m = 3 \leftrightarrow 4$, while the second one from the left relates to the Zeeman transition $m = 2 \leftrightarrow 3$.

of the photocurrent signal with respect to the oscillating magnetic field in phase with cos (ωt), given by [35]

$$\begin{aligned} J_{ip} &\propto -\frac{\gamma\,(B_c\Delta + B_s\Gamma)/2}{\Delta^2 + \Gamma^2 + \gamma^2\left(B_c^2 + B_s^2\right)/4}, \\ J_{qu} &\propto \frac{\gamma\,(B_s\Delta - B_c\Gamma)/2}{\Delta^2 + \Gamma^2 + \gamma^2\left(B_c^2 + B_s^2\right)/4}. \end{aligned} \tag{1}$$

Here $\Delta = \omega - \omega_L$ is the detuning of the applied rf frequency from the Larmor frequency, $\Gamma = \Gamma_{\mathrm{p}} + \Gamma_{pr} + \Gamma_{\mathrm{dark}}$, Γ_{p} is the optical pumping rate, Γ_{pr} is the atomic decoherence rate due to the probe light, and Γ_{dark} is the decay rate in the absence of light. Therefore, we can extract the information of $\mathbf{B}_{\mathrm{rf}}$ by demodulating the photocurrent signal with a lock-in amplifier (LIA).

We use the rf OPM to detect small containers with salt water using the principle of electromagnetic induction. The electrical conductivity σ of the salt water can be varied by changing the concentration of salt. At low concentrations, salt water is a good model sample for body tissue. A primary oscillating magnetic field $\mathbf{B}_{\mathrm{p}}$ created by a small coil denoted “primary field coil” induces eddy currents in the salt water. This in turn generates a small secondary oscillating magnetic field $\mathbf{B}_{\mathrm{ed}}$, which is detected with the magnetometer. When the thickness t of the object is much smaller than the skin depth $d \approx \sqrt{2/(\mu_0\sigma\omega)}$, which characterizes the attenuation of the primary field penetrating into the object, the secondary field is 90° out of phase with the primary field [41]. Here μ_0 is the vacuum permeability. Without loss of generality, we assume $\mathbf{B}_{\mathrm{p}} = B_{\mathrm{p}}\cos(\omega t)\,\hat{\mathbf{y}}$ and correspondingly, $\mathbf{B}_{\mathrm{ed}} = B_{\mathrm{ed}}\sin(\omega t)\,\hat{\mathbf{y}}$. Then by replacing B_c with B_{p}, and replacing B_s with B_{ed} in Eq. (1), we can get the expression for the two quadrature outputs of LIA, corresponding to the in-phase and out-of-phase components, respectively.

To avoid detecting the small secondary magnetic field on the top of a large primary field, we apply a compensation field using a small coil denoted “compensation coil” such that the total primary oscillating field is zero at the vapor-cell position in the absence of the salt-water container. The container is placed on the top of the primary field coil. It is further away from the compensation coil, such that the eddy current generated by it can be ignored. In such a condition ($B_{\mathrm{p}} = 0$), the outputs of LIA are

$$\begin{aligned} Y &\propto -\frac{\gamma B_{\mathrm{ed}}\Gamma/2}{\Delta^2 + \Gamma^2 + \gamma^2 B_{\mathrm{ed}}^2/4}, \\ X &\propto \frac{\gamma B_{\mathrm{ed}}\Delta/2}{\Delta^2 + \Gamma^2 + \gamma^2 B_{\mathrm{ed}}^2/4}. \end{aligned} \tag{2}$$

We can see that the X has a dispersive shape and is linear with B_{ed} when the conductivity of the object is small. We have previously shown that this differential technique gives a large improvement in the signal-to-noise ratio of around three orders of magnitude when detecting low-conductivity samples [35].

III. PRINCIPLE DESCRIPTION

A. Nonlinear Zeeman effect

An alkaline atom in an S level (orbital angular momentum $L = 0$) in an external magnetic field $\mathbf{B}$ is described by the Hamiltonian

$$\hat{H} = A_h\mathbf{I}\cdot\mathbf{S} + g_s\mu_B\mathbf{S}\cdot\mathbf{B} - g_I\mu_N\mathbf{I}\cdot\mathbf{B}, \tag{3}$$

where A_h is the hyperfine coupling constant, g_s and g_I are the electron-spin and nuclear Land*é* factors, **I** and **S** are the nuclear and electron spins, μ_B is the Bohr magneton, and μ_N is the nuclear magneton. The first term describes the hyperfine interaction and the last two terms describe interactions of electron and nuclear spins with the magnetic field. The energy of the sublevel $|F,m\rangle$ is given by

$$E_m = -\frac{h\nu_{\mathrm{hfs}}}{2\,(2I+1)} - g_I\mu_N Bm \pm \frac{h\nu_{\mathrm{hfs}}}{2}\sqrt{1 + \frac{4mx}{2I+1} + x^2}, \tag{4}$$

where h is Planck’s constant, ν_{hfs} is the hyperfine splitting, $x = (g_s\mu_B + g_I\mu_N)\,B/h\nu_{\mathrm{hfs}}$, and ± is used for $F = I \pm 1/2$. For the cesium atom [42] in the $6^2S_{1/2}F = 4$ level, expanding the eigenenergies and keeping the second-order term of B, we obtain the transition frequency between two adjacent Zeeman levels [43]

$$\frac{E_{m+1} - E_m}{h} = \nu_L - \frac{2\nu_L^2}{\nu_{\mathrm{hfs}}}\left(m + \frac{1}{2}\right), \tag{5}$$

where $\nu_L = \omega_L/2\pi = \gamma B/2\pi$. The Zeeman resonance frequencies are thus nonlinearly dependent on the magnetic field. The quadratic effect, which results in different resonance frequencies of the Zeeman transitions, is

$$\nu_{\mathrm{QZ}} = \frac{2\nu_L^2}{\nu_{\mathrm{hfs}}}. \tag{6}$$

Sweeping the frequency of the transverse rf field, the so-called magneto-optical resonance signal (MORS), which contains $2F$ magnetic resonance lines, can be observed when the linewidths are much smaller than the quadratic splitting. The intensities of eight peaks give the population difference between two adjacent Zeeman energy levels and therefore give a method for obtaining the polarization of the atomic ensemble [43,44]. Applying an rf field via the primary field coil and the compensation coil in the Helmholtz mode, the MORSs of our cesium vapor cell with spin polarization of 81.3% and 96.4% are recorded without and with the pump beam, respectively [see Figs. 1(b) and 1(c)]. The operating frequency of our experiment is in the vicinity of 1.93 MHz corresponding to a quadratic Zeeman splitting of around 810 Hz. A narrow linewidth of the MORS (around 30 Hz) has been achieved by using a paraffin-coated vapor cell [45,46]. As the linewidth is much smaller than the quadratic Zeeman splitting, the $2F = 8$ magnetic resonances are well resolved in Figs. 1(b) and 1(c).

B. Single-species dual-frequency magnetometer and bias magnetic field stabilization

Here we propose and demonstrate a construction of an atomic magnetometer that is able to simultaneously measure dc and rf magnetic fields, using ^{133}Cs as the only sensing substance. From the MORS shown in Fig. 1, we can see that different Zeeman transitions can be independently controlled due to the good spectral resolution of the system. Therefore, the rf field resonant with transition $m = 2 \leftrightarrow 3$ ($T_{2\leftrightarrow3}$) or $m = 3 \leftrightarrow 4$ ($T_{3\leftrightarrow4}$) does not affect the other transition. The idea behind the magnetometer is to use the resonance signal of $T_{2\leftrightarrow3}$ to measure the dc magnetic field, and to measure the rf magnetic field via the resonance signal of $T_{3\leftrightarrow4}$. In the context of constructing a stable atomic magnetic induction sensor, we can extract the eddy-current information by $T_{3\leftrightarrow4}$, while monitoring and compensating the drift of bias magnetic field by $T_{2\leftrightarrow3}$.

In the setup shown in Fig. 1, the primary field coil and the compensation coil are used to drive $T_{3\leftrightarrow4}$, while the auxiliary coil is used to drive $T_{2\leftrightarrow3}$. The optoelectronic signal from the balanced detector is fed to a dual-channel digital LIA. The signal is demodulated with the applied rf fields driving $T_{3\leftrightarrow4}$ in channel 1 and is demodulated with the rf field driving $T_{2\leftrightarrow3}$ in channel 2. The demodulated output from channel 2 is used as an error signal for the following servo system, consisting of a proportional module and a pair of compensation coils.

To test the improved stability of the sensor, a weak field (0.75 nT) is added by the primary field coil and the compensation coil. The reference phase of LIA is tuned in such a way that its Y output demodulates the in-phase signal. At the resonance condition, the Y output of channel 1 on the LIA serves as the reference point for detecting the rf field generated by the eddy current. The feedback parameter of the servo system is adjusted by optimizing the Allan deviation of the signal. Figure 2(a) shows the atomic response signals to the resonant rf field with and without the bias magnetic field feedback and Fig. 2(b) shows the corresponding Allan deviations. The vapor cell is coated by antirelaxation material for narrow broadening of the magnetic resonance spectra. It allows higher sensitivity for measuring an rf field, while also making the sensor more sensitive to the drift of the bias magnetic field. Without the compensation system, the detuning Δ resulting from the current drift would drive the sensor out of the linear response range on the scale of hundreds of seconds. The compensation system can greatly suppress the degradation caused by the drift. On the long-term scale, almost 2 orders of improvement can be achieved with the active stabilization scheme. Therefore, rewards from the long-term average of the data are allowed.

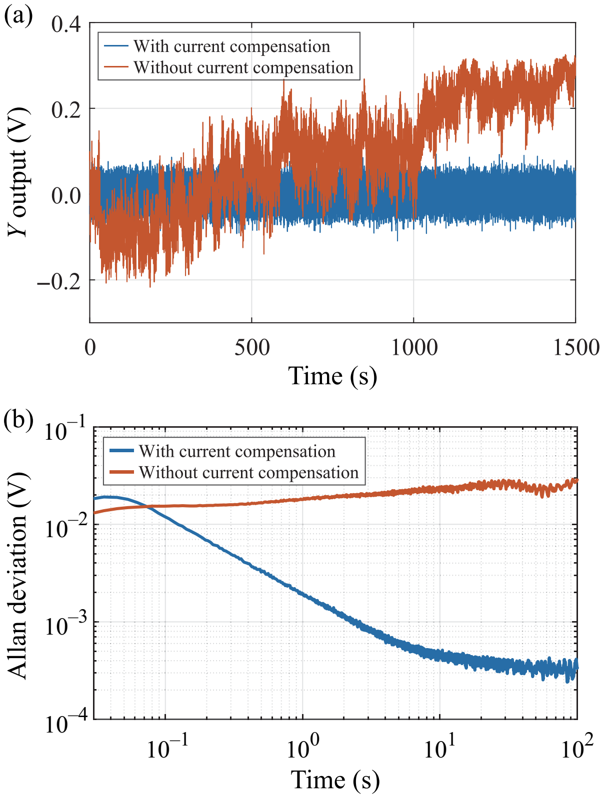

FIG. 2. Stabilization effect of the scheme. (a) Y output of channel 1 of LIA at the resonance condition with and without the feedback system. (b) Allan deviations of the data shown in (a).

IV. OPTIMIZATION OF SETUP PARAMETERS

A. Figure of merit for optimizing MIT parameters

In many MIT applications, the secondary magnetic field is small and the condition $B_{\mathrm{ed}} \ll \Gamma/\gamma$ is valid. For example, B_{ed} is in the order of several picoteslas in MIT of the heart. Therefore, the expression for eddy-current signal under the resonant condition, shown as Eq. (2), can be further simplified to

$$Y_{\mathrm{ed}} = -\frac{\gamma A}{2\Gamma} B_{\mathrm{ed}}, \tag{7}$$

where A is a proportionality constant related to atomic density, optical, and electronic parameters. We can define a figure of merit for evaluating the signal induced by the eddy-current magnetic field B_{ed} as

$$\mathcal{M} = \frac{\gamma A}{2\Gamma}. \tag{8}$$

Under the resonant condition, applying a test magnetic field $\mathbf{B}_t = B_t \cos(\omega t)\,\hat{\mathbf{y}}$ for optimizing $\mathcal{M}$, the in-phase components of the PD signal with respect to B_t ($\gamma B_t \ll \Gamma$) can be written as

$$X_t = -\frac{\gamma A \Gamma B_t}{2\left(\Delta^2 + \Gamma^2 + \gamma^2 B_t^2/4\right)} \approx -\frac{\gamma A}{2\Gamma} B_t = -\mathcal{M} B_t. \tag{9}$$

Therefore, the optimization problem of $\mathcal{M}$ is equivalent to optimizing the X output of LIA when a small test resonant ac field is applied. It also corresponds to maximizing the peak value of the in-phase component of the MORS.

B. Optimization of pump power and atomic density

Increasing the pump power will create higher atomic polarization, thereby increasing A in Eq. (8). However, more pump power also results in more pump-power broadening, i.e., in a larger Γ in Eq. (8). The increase in atomic density has a similar effect. As we increase the vapor-cell temperature, more atoms would contribute to the signal, while the higher spin-exchange collision rate would degrade the gain. Therefore, there is optimal pump power and atomic density for the optimal performance of the OPM. A weak test magnetic field with $B_t = 0.38$ nT was applied through the primary field coil and the compensation coil to optimize the pump power and atomic density, while the auxiliary coil was blocked. The results are shown in Fig. 3 leading to the choice of the pump light power 0.5 uW and the atomic density 28×10^{16} m^{-3} (around 42 °C). In our experiment, we employed atomic absorption spectroscopy to measure and subsequently fit the atomic density, thus obtaining a determination of its value. During the implementation of the optimization process, a repump power of 67 uW was utilized, which proved to be sufficiently high to effectively deplete the atoms in $F = 3$ to a significant extent. The probe laser with a power of 56 uW is locked with a detuning of 1.95 GHz from the $F = 4 \rightarrow F' = 4, 5$ crossover transition of the D2 line. After calibrating the rf coils, we determined a coefficient of 37.8 nT/V for converting the set amplitude of the function generator to the rf magnetic field. We finally got $\mathcal{M} = 1.53$ V/nT.

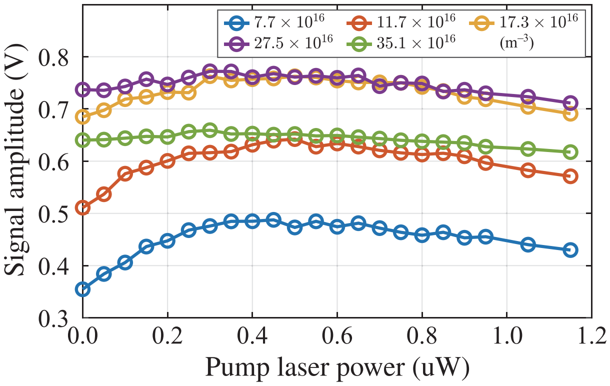

FIG. 3. Optimization of the pump light power and atomic density. Different colors are used to distinguish results under different atomic densities.

C. Optimization of primary field

The secondary field from the eddy current is proportional to the amplitude of the primary field. However, in the actual situation, we can hardly perfectly cancel two rf fields in the whole space occupied by the vapor cell due to the spatial inhomogeneity of the rf fields. Therefore, increasing rf amplitude would still broaden the atomic resonance linewidth, though the linewidth is significantly suppressed by the differential configuration, where the two rf fields compensate each other in the center.

To explore the influence of the primary field $\mathbf{B}_\mathrm{p}$, we varied its amplitude B_p and observed the change in the linewidth of the MORS. For each amplitude value, the amplitude and phase of the compensation field from rf the compensation coil were correspondingly adjusted by minimizing the offset of the output signal of LIA. A small oscillating magnetic field B_t' is applied through rf the auxiliary coil to induce the transverse atomic polarization vector. The frequency of B_t' is swept for the MORS. It is noteworthy that the amplitude of B_t' is varied proportionally to the amplitude of $\mathbf{B}_\mathrm{p}$ due to the fact that the secondary field is proportional to the primary field. By doing this, we optimize $\mathbf{B}_\mathrm{p}$ aiming at an optimal eddy-current signal. Under different amplitudes of $\mathbf{B}_\mathrm{p}$, the measured MORS, as well as the amplitude and linewidth of the resonance peak are presented in Fig. 4. We can see the signal of the atomic magnetometer is gradually saturated as B_p increases. The coincidence between the experimental result and the fitting function $cU/\left(1 + [U/U_\mathrm{sat}]^2\right)$ indicates the saturation comes from the rf broadening. Here U is the set amplitude on the function generator for the primary field. c and U_sat are fitting parameters. The rising tendency of the linewidth, described well by the function $\sqrt{aU^2 + b}$, also gives direct evidence of the rf broadening. Here a and b are fitting parameters. To mitigate issues related to high rf broadening, we set the amplitude to 800 mV, corresponding to a magnetic field amplitude of 30.2 nT, for the subsequent sample measurements.

V. MIT RESULTS

We detect salt-water samples with conductivities $\sigma = 0.55, 1.04, 1.98, 3.78, 6.84, 10.7$ S/m. The salt water is inside a 3D-printed container with the size of (2 cm)^3 corresponding to 8 ml of salt water. The conductivity of the salt water is calibrated using a commercial conductivity meter (Hanna Instruments HI98192). The container is scanned in the x direction above the primary field coil using a motorized translation stage. The rod connecting

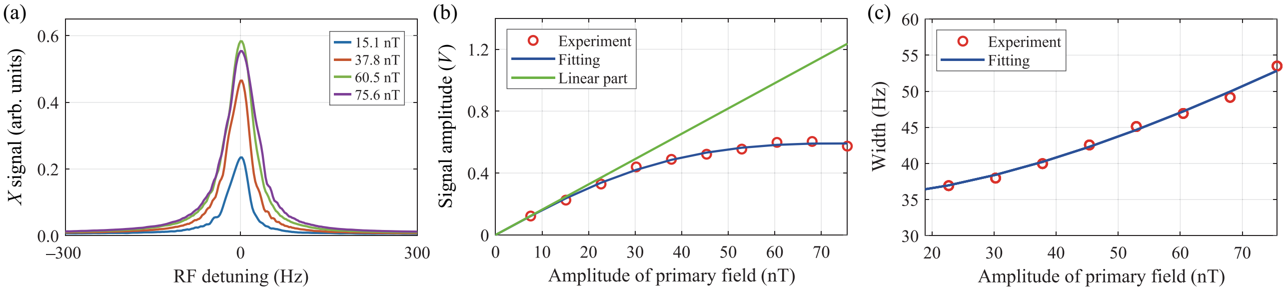

FIG. 4. The influence of the amplitude of the primary field on the atomic resonance signal. (a) The raw spectra of the measured atomic resonance signal of Zeeman transition $m = 3 \leftrightarrow 4$ for the varied amplitudes of $\mathbf{B}_p$. (b) Dependence of the signal amplitude on the amplitude of $\mathbf{B}_p$. Data are shown together with a fit to the function $cU/\left(1+[U/U_{sat}]^2\right)$ (blue curve) and linear part of the fit function cU (green line). (c) Dependence of atomic resonance width on the amplitude of $\mathbf{B}_p$. Data are shown together with a fit to the function $\sqrt{aU^2+b}$ (blue curve).

the container and the stage is also nonmagnetic. The container is moved back and forth along a path of 5 cm with a speed of 1 mm/s. At the beginning and end of the path, the acceleration is ±0.5 mm^2/s. The LIA output signal is acquired with a sampling rate of 112 Hz. All trigger signals to accelerate the container are recorded for averaging.

The detected sample signals are shown in Fig. 5(a) (average number $N_{avg} = 150$) and Fig. 5(b) ($N_{avg} = 60$). Here N_{avg} refers to the number of times the container is scanned over the primary field coil. The dip of the signal appears at the center of the path, where the sample is closest to both the primary coil and the vapor cell. Considering the dip depth as the signal amplitude, a linear relationship is found between the signal intensity and the conductivity [Fig. 5(c)]. It verifies the feasibility of the setup to extract the conductivity information of the measured samples. We also get the scale factor as $F = -1.19$ mV/(S/m) from Fig. 5(c). The noise-equivalent conductivity (NEC) can be defined as $\Delta\sigma = \Delta V/|F|$, where ΔV is the standard deviation (STD) of the output voltage from the lock-in amplifier.

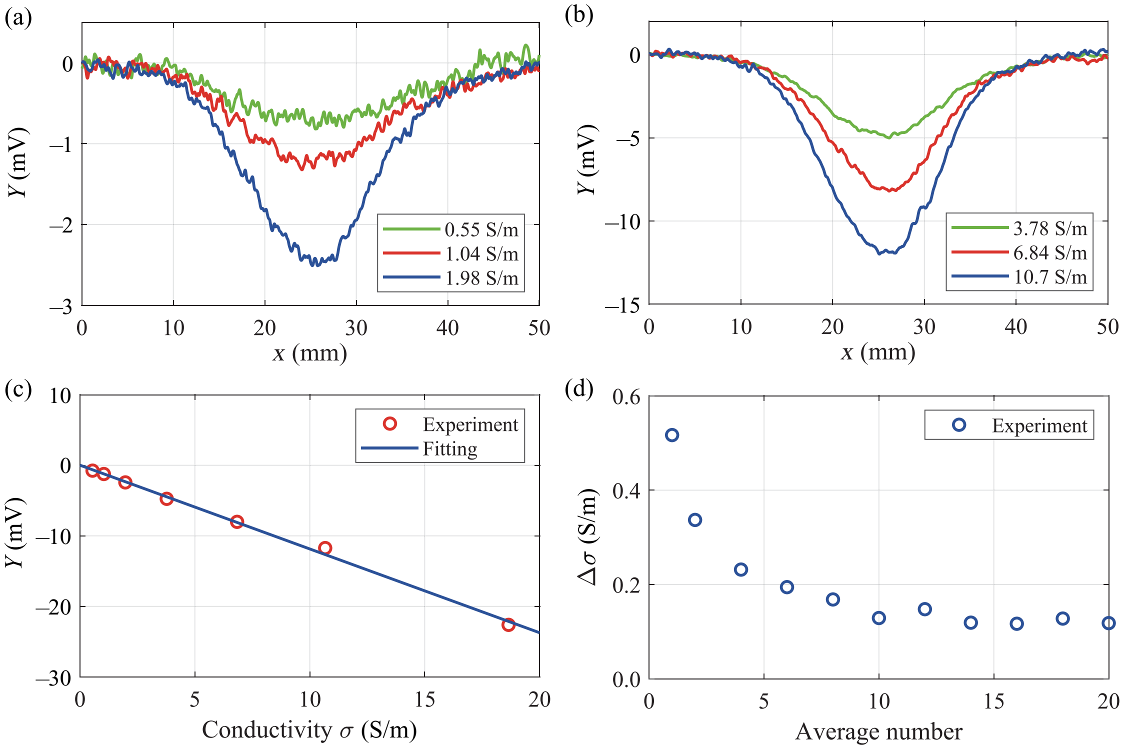

FIG. 5. Detection of salt water with different conductivities. (a) 150 averages. (b) 60 averages. (c) Detected relative change in signal between position $x = 0$ mm and $x = 25$ mm as a function of conductivity. The blue line shows the linear fit. (d) NEC for the salt-water sample of $\sigma = 1$ S/m as a function of the average number of the scan signal traces.

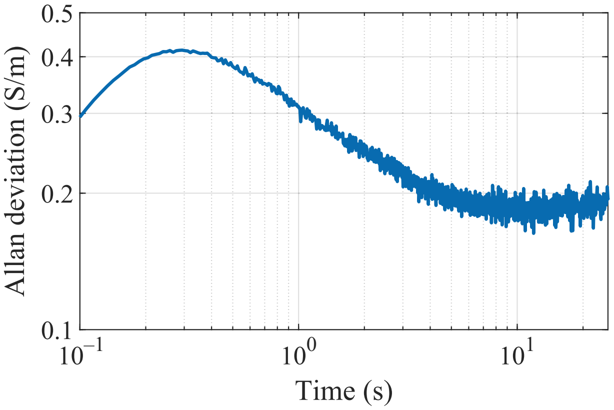

FIG. 6. Allan deviation from the static test results for the salt-water sample of 10.7 S/m. During data recording, the time constant of the lock-in amplifier was set to 100 ms.

To analyze NEC, we record 240 traces of the scan signal. NEC is determined by calculating the STD of the dip values across various averaging counts, where trace signals are averaged together. Figure 5(d) shows NEC for the salt-water sample of $\sigma = 1$ S/m as a function of the average number N_{avg}. For a single trace, the estimated NEC is 0.52 S/m. When $N_{\text{avg}} = 2$, the NEC decreases to 0.34 S/m, and with $N_{\text{avg}} = 10$, it further reduces to 0.13 S/m.

In addition to obtaining conductivity data by scanning the sample over the sensor, we can also determine conductivity using static tests. For this approach, we position the sample directly above the sensor and capture the signal over a certain duration. Conductivity is then assessed by adjusting for the zero offset, which we determine by placing the sample at a distance from the sensor. The Allan deviation of these measurements is depicted in Fig. 6. By averaging the signal for 10 s, we can achieve an NEC of 0.18 S/m.

VI. CONCLUSIONS

In conclusion, we have demonstrated a comagnetometer with ^{133}Cs as the only sensing element. It uses two Zeeman transitions to measure both static and oscillating magnetic fields simultaneously. In our experiment, it works as a self-stabilized sensor for detecting weak eddy currents. The sensor's enhanced long-term stability leads to a significant improvement in detecting low-conductivity objects, resulting in higher sensitivity. In this work, our dual-frequency atomic magnetometer was operated in a relatively quiet magnetic environment inside a magnetic shield. We expect that our method will also work well in unshielded conditions where there is more environmental magnetic noise. In that case, it may be beneficial to simultaneously use fluxgate magnetometers and our comagnetometer method for stabilizing the bias magnetic field. Recently, a quantum-enhanced version of the atomic MIT was demonstrated [47]. By integrating these technologies, we can significantly enhance the capabilities of magnetic induction tomography and make significant progress in detecting eddy currents in human tissue.

ACKNOWLEDGMENTS

This work was supported by the Novo Nordisk Foundation (Grants No. NNF20OC0064182, No. NNF24SA0088433), by the European Research Council (ERC) under the Horizon 2020 (Grant Agreement No. 787520) and by VILLUM FONDEN under a Villum Investigator Grant No. 25880. W.Z. and H.W. acknowledge the support of the National Nature Science Foundation of China (Grants No. 12075206, No. 11905184).

[1] I. K. Kominis, T. W. Kornack, J. C. Allred, and M. V. Romalis, A subfemtotesla multichannel atomic magnetometer, Nature **422**, 596 (2003).

[2] D. Budker and M. Romalis, Optical magnetometry, Nat. Phys. **3**, 227 (2007).

[3] D. Budker and D. F. Jackson Kimball, *Optical Magnetometry* (Cambridge University Press, Cambridge, UK, 2013).

[4] H. Xia, A. Ben-Amar Baranga, D. Hoffman, and M. V. Romalis, Magnetoencephalography with an atomic magnetometer, Appl. Phys. Lett. **89**, 211104 (2006).

[5] E. Boto, N. Holmes, J. Leggett, G. Roberts, V. Shah, S. S. Meyer, L. D. Muñoz, K. J. Mullinger, T. M. Tierney, S. Bestmann *et al.*, Moving magnetoencephalography towards real-world applications with a wearable system, Nature **555**, 657 (2018).

[6] G. Bison, N. Castagna, A. Hofer, P. Knowles, J.-L. Schenker, M. Kasprzak, H. Saudan, and A. Weis, A room temperature 19-channel magnetic field mapping device for cardiac signals, Appl. Phys. Lett. **95**, 173701 (2009).

[7] R. Wyllie, M. Kauer, R. T. Wakai, and T. G. Walker, Optical magnetometer array for fetal magnetocardiography, Opt. Lett. **37**, 2247 (2012).

[8] O. Alem, T. H. Sander, R. Mhaskar, J. LeBlanc, H. Eswaran, U. Steinhoff, Y. Okada, J. Kitching, L. Trahms, and S. Knappe, Fetal magnetocardiography measurements with an array of microfabricated optically pumped magnetometers, Phys. Med. Biol. **60**, 4797 (2015).

[9] W. Q. Zheng, S. R. Su, G. Y. Zhang, X. Bi, and Q.g Lin, Vector magnetocardiography measurement with a compact elliptically polarized laser-pumped magnetometer, Biomed. Opt. Express **11**, 649 (2020).

[10] S. Zuo, H. Heidari, D. Farina, and K. Nazarpour, Miniaturized magnetic sensors for implantable magnetomyography, Adv. Mater. Technol. **5**, 2000185 (2020).

[11] G. Z. Iwata, Y. Hu, A. Wickenbrock, T. Sander, M. Muthuraman, V. C. Chirumamilla, S. Groppa, Q. Liu, and D. Budker, Biomagnetic signals recorded during transcranial magnetic stimulation (TMS)-evoked peripheral muscular activity, Biomed. Eng.-Biomed. Tech. **67**, 333 (2022).

[12] B. U. Westner, J. I. Lubell, M. Jensen, S. Hokland, and S. S Dalal, Contactless measurements of retinal activity

using optically pumped magnetometers, NeuroImage **243,** 118528 (2021).

[13] K. Jensen, R. Budvytyte, R. A. Thomas, T. Wang, A. M. Fuchs, M. V. Balabas, G. Vasilakis, L. D. Mosgaard, H. C. Stærkind, J. H. Müller *et al.*, Non-invasive detection of animal nerve impulses with an atomic magnetometer operating near quantum limited sensitivity, Sci. Rep. **6,** 29638 (2016).

[14] Y. Bu, J. Prince, H. Mojtahed, D. Kimball, V. Shah, T. Coleman, M. Sarkar, R. Rao, M. Huang, P. Schwindt *et al.*, Peripheral nerve magnetoneurography with optically pumped magnetometers, Front. Physiol. **13,** 798376 (2022).

[15] W. Wasilewski, K. Jensen, H. Krauter, J. J. Renema, M. V. Balabas, and E. S. Polzik, Quantum noise limited and entanglement-assisted magnetometry, Phys. Rev. Lett. **104,** 133601 (2010).

[16] I. M. Savukov, S. J. Seltzer, M. V. Romalis, and K. L. Sauer, Tunable atomic magnetometer for detection of radio-frequency magnetic fields, Phys. Rev. Lett. **95,** 063004 (2005).

[17] W. Chalupczak, R. M. Godun, S. Pustelny, and W. Gawlik, Room temperature femtotesla radio-frequency atomic magnetometer, Appl. Phys. Lett. **100,** 242401 (2012).

[18] H. Griffiths, W. R. Stewart, and W. Gough, Magnetic induction tomography: A measuring system for biological tissues, Ann. N. Y. Acad. Sci. **873,** 335 (1999).

[19] H. Griffiths, Magnetic induction tomography, Meas. Sci. Technol. **12,** 1126 (2001).

[20] A. Korjenevsky, V. Cherepenin, and S. Sapetsky, Magnetic induction tomography: Experimental realization, Physiol. Meas. **21,** 89 (2000).

[21] H. Wei and M. Soleimani, Hardware and software design for a national instrument-based magnetic induction tomography system for prospective biomedical applications, Physiol. Meas. **33,** 863 (2012).

[22] L. Ma and M. Soleimani, Magnetic induction tomography methods and applications: A review, Meas. Sci. Technol. **28,** 072001 (2017).

[23] J. R. Feldkamp, Single-coil magnetic induction tomographic three-dimensional imaging, J. Med. Imaging (Bellingham) **2,** 013502 (2015).

[24] A. Wickenbrock, S. Jurgilas, A. Dow, L. Marmugi, and F. Renzoni, Magnetic induction tomography using an all-optical ^{87}Rb atomic magnetometer, Opt. Lett. **39,** 6367 (2014).

[25] A. Wickenbrock, N. Leefer, J. W. Blanchard, and D. Budker, Eddy current imaging with an atomic radio-frequency magnetometer, Appl. Phys. Lett. **108,** 183507 (2016).

[26] G. Bevilacqua, V. Biancalana, Y. Dancheva, A. Fregosi, G. Napoli, and A. Vigilante, Electromagnetic induction imaging: Signal detection based on tuned-dressed optical magnetometry, Opt. Express **29,** 37081 (2021).

[27] P. Bevington, R. Gartman, and W. Chalupczak, Enhanced material defect imaging with a radio-frequency atomic magnetometer, J. Appl. Phys. **125,** 094503 (2019).

[28] P. Bevington, R. Gartman, D. J. Botelho, R. Crawford, M. Packer, T. M. Fromhold, and W. Chalupczak, Object surveillance with radio-frequency atomic magnetometers, Rev. Sci. Instrum. **91,** 055002 (2020).

[29] N. Papi, E. Cali, C. Marinelli, E. Mariotti, and V. Millucci, Edge detection in atomic magnetometer imaging, J. Siena Acad. Sci. **10,** 1 (2018).

[30] B. Maddox, Y. Cohen, and F. Renzoni, Through-skin pilot-hole detection and localization with a mechanically translatable atomic magnetometer, Appl. Phys. Lett. **120,** 014002 (2022).

[31] R. Gartman and W. Chalupczak, Identification of object composition with magnetic inductive tomography, Rev. Sci. Instrum. **92,** 115001 (2021).

[32] C. Deans, L. Marmugi, and F. Renzoni, Active underwater detection with an array of atomic magnetometers, Appl. Opt. **57,** 2346 (2018).

[33] L. M. Rushton, T. Pyragius, A. Meraki, L. Elson, and K. Jensen, Unshielded portable optically pumped magnetometer for the remote detection of conductive objects using eddy current measurements, Rev. Sci. Instrum. **93,** 125103 (2022).

[34] L. Marmugi and F. Renzoni, Optical magnetic induction tomography of the heart, Sci. Rep. **6,** 23962 (2016).

[35] K. Jensen, M. Zugenmaier, J. Arnbak, H. Stærkind, M. V. Balabas, and E. S. Polzik, Detection of low-conductivity objects using eddy current measurements with an optical magnetometer, Phys. Rev. Res. **1,** 033087 (2019).

[36] C. Deans, L. Marmugi, and F. Renzoni, Sub-Sm^{-1} electromagnetic induction imaging with an unshielded atomic magnetometer, Appl. Phys. Lett. **116,** 133501 (2020).

[37] C. Deans, L. Marmugi, and F. Renzoni, Sub-picotesla widely tunable atomic magnetometer operating at room-temperature in unshielded environments, Rev. Sci. Instrum. **89,** 083111 (2018).

[38] L. Marmugi, C. Deans, and F. Renzoni, Electromagnetic induction imaging with atomic magnetometers: Unlocking the low-conductivity regime, Appl. Phys. Lett. **115,** 083503 (2019).

[39] T. Pyragius and K. Jensen, A high performance active noise control system for magnetic fields, Rev. Sci. Instrum. **92,** 124702 (2021).

[40] J. E. Dhombridge, N. R. Claussen, J. Iivanainen, and P. D. D. Schwindt, High-sensitivity rf detection using an optically pumped comagnetometer based on natural-abundance rubidium with active ambient-field cancellation, Phys. Rev. Appl. **18,** 044052 (2022).

[41] H. Griffiths, W. Gough, S. Watson, and R. J. Williams, Residual capacitive coupling and the measurement of permittivity in magnetic induction tomography, Physiol. Meas. **28,** S301 (2007).

[42] D. A. Steck, Cesium D Line Data, https://steck.us/alkalidata/ (2019).

[43] B. Julsgaard, Entanglement and quantum interactions with macroscopic gas samples, PhD Thesis, University of Aarhus, 2003.

[44] B. Julsgaard, J. Sherson, J. L. Sørensen, and E. S. Polzik, Characterizing the spin state of an atomic ensemble using the magneto-optical resonance method, J. Opt. B: Quantum Semiclassical Opt. **6,** 5 (2003).

[45] M. V. Balabas, K. Jensen, W. Wasilewski, H. Krauter, L. S. Madsen, J. H. Müller, T. Fernholz, and E. S. Polzik, High quality anti-relaxation coating material for alkali atom vapor cells, Opt. Express **18,** 5825 (2010).

[46] M. V. Balabas, T. Karaulanov, M. P. Ledbetter, and D. Budker, Polarized alkali-metal vapor with minute-long transverse spin-relaxation time, Phys. Rev. Lett. **105**, 070801 (2010).

[47] Wenqiang Zheng, Hengyan Wang, Rebecca Schmieg, Alan Oesterle, and Eugene S. Polzik, Entanglement-enhanced magnetic induction tomography, Phys. Rev. Lett. **130**, 203602 (2023).